RSC Advances

ROYAL SOCIETY OF CHEMISTRY

www.rsc.org/advances

RSC Advances

ARTICLE

Mesoporous transition metal dichalcogenide ME$_2$ (M = Mo, W; E = S, Se) with 2-D layered crystallinity as anode materials for lithium ion batteries†

Yoon Yun Lee,[a] Gwi Ok Park,[b] Yun Seok Choi,[c] Jeong Kuk Shon,‡[c] Jeongbae Yoon,[b] Kyoung Ho Kim,[c] Won-Sub Yoon,*[b] Hansu Kim,*[d] and Ji Man Kim*[abc]

Mesoporous transition metal dichalcogenides (TMDCs), comprised of group VI metals (Mo and W) and chalcogens (S and Se), with 2-D layered crystalline frameworks and 3-D pore structures were successfully prepared *via* a melting-infiltration assisted nano-replication method using a mesoporous template KIT-6 with cubic *Ia*3*d* symmetry. A combined analysis using X-ray diffraction, N$_2$ adsorption-desorption and electron microscopy indicated that the mesoporous TMDCs, thus obtained, exhibited high surface areas (87 − 105 m^2·g^{-1}), large pore volumes (0.21 − 0.25 cm^3·g^{-1}) and well-defined mesopores of about 20 nm in diameters. The mesoporous TMDCs showed outstanding rate capabilities up to 2C as well as high reversible lithium storage capacities (MoS$_2$ 710 mAh·g^{-1}; MoSe$_2$ 744 mAh·g^{-1}; WS$_2$ 501 mAh·g^{-1}; WSe$_2$ 427 mAh·g^{-1}) without a remarkable fading of capacity.

1. Introduction

Due to their high energy and power densities, lithium ion batteries (LIBs) are becoming the most important power sources for portable devices and electric vehicles (EVs).[1-4] However, commercial LIBs (comprised of lithium metal oxide cathode and carbonaceous anode) are not as sufficient as high power sources for EVs, because of their low lithium storage capacities caused by one or less electron transfer reactions of electrode materials (*e.g.* six carbon atoms in graphite react with only one Li$^+$).[5-7] In order to accomplish sufficiently high energy and power densities, is necessary to develop novel electrode materials that can exhibit multi-electron transfer reactions with high lithium storage capacity.[6, 7]

Carbonaceous materials are the mostly used anode material for LIBs due to their low working voltage, low cost, good stability and long cycle life.[7-10] Because of low theoretical capacity (LiC$_6$, 372 mAh·g^{-1}), novel materials such as alloys, metal oxides, metal phosphides and metal sulphides have been investigated as alternative anode materials for LIB anode.[4, 11-24] Unfortunately, these materials have some limits in their practical application such as low coulombic efficiency, high irreversible capacity, high cost, unstable solid electrolyte interphase (SEI) layer formation, and short life cycle.[7]

Transition metal dichalcogenides (TMDCs), composed of group IV–VI transition metals and chalcogens (S, Se and Te), with graphite-like layered crystalline frameworks are expected to have great potential in nano-electronics, sensing, catalysis, energy storage and harvesting.[25-32] In particular, due to the interesting intercalation chemistry caused by their layered crystal structures, group VI metal (Mo and W) based TMDCs have been investigated as anode materials for LIBs.[33-38] Indeed, TMDCs are being regarded as promising candidates for LIB anodes because of high reversible capacity and an excellent rate capability.[39]

Mesoporous materials, exhibiting well-defined mesopore sizes and nano-sized wall-thicknesses, have some advantages as electrode materials for LIBs: 1) the buffer effect by their cavities (mesopores) for volume change during the charge-discharge processes, 2) controllable mesopore size and connectivity that offer a short diffusion pathway for the electrolyte and transport of lithium ions into the surface of the material, 3) shortening of the solid-state diffusion path for the lithium ion into the material by their nano-sized framework (usually < 10 nm), and 4) large electrochemically active surface area between the electrode material and the electrolyte. Accordingly, mesoporous materials with inorganic frameworks such as carbons and metal oxides have been widely investigated as electrode material for LIBs.[40-53] However, due to the lack of suitable precursors, a major challenge for preparing high quality mesoporous TMDCs is to find a suitable and facile synthesis route. There are only a few examples of mesoporous TMDCs, MoS$_2$, MoSe$_2$ WS$_2$ and WSe$_2$, were synthesized *via* the nano-replication method, which is well-known for preparing ordered mesoporous materials, using 2-D hexagonal *P*6*mm* SBA-15 as a hard-template with direct or *in-situ* generated H$_2$S and H$_2$Se gases as reducing agents.[54-59] To the best of our knowledge, there have been no reports on applications of ordered mesoporous TMDCs with 3-D pore channel systems for LIB electrodes.

[a.] SKKU Advanced Institute of Nanotechnology (SAINT), Sungkyunkwan University, Suwon 16419, Republic of Korea.
[b.] Department of Energy Science, Sungkyunkwan University, Suwon 16419, Republic of Korea. E-mail: wsyoon@skku.edu
[c.] Department of Chemistry, Sungkyunkwan University, Suwon 16419, Republic of Korea. E-mail: jimankim@skku.edu; Fax +82 31 299 4174; Tel +82 31 290 5930
[d.] Department of Energy Engineering, Hanyang University, Seoul 04763, Republic of Korea. E-mail: khansu@hanyang.ac.kr
† Electronic Supplementary Information (ESI) available: XRD patterns, SEM and TEM images of KIT-6 silica template and bulk MoS$_2$ are depicted. Charge-discharge profiles of mesoporous TMDCs at various C-rates also could be confirmed in ESI. See DOI: 10.1039/x0xx00000x
‡ Present Address: Energy Lab., Samsung Advanced Institute of Technology (SAIT), Samsung Electronics Co., Ltd., P.O. Box 111, Suwon 16678, Republic of Korea.

ARTICLE

In the present work, mesoporous TMDCs with 3-D pore channel systems and crystalline frameworks of MoS_2, $MoSe_2$, WS_2 and WSe_2 were successfully prepared *via* the nano-replication method with a melting-infiltration of chalcogen (S or Se) powders using the 3-D bicontinuous cubic *Ia*3*d* KIT-6 silica template (Fig. 1). The mesoporous TMDCs, exhibiting ordered 3-D mesostructures with layered crystalline framework structures, show high surface areas, large pore volumes, high reversible electrochemical lithium storage capacities, and outstanding rate capabilities up to 2C.

2. Experimental

2.1 Preparation of KIT-6 template

Ordered mesoporous silica (OMS) template KIT-6 exhibiting 3-D bicontinuous cubic *Ia*3*d* mesostructures was prepared using Pluronic® P-123 block copolymer as the template and tetraethyl orthosilicate (TEOS) as the silica source. The Pluronic® P-123 block copolymer was dissolved in *n*-butanol solvent, and distilled water was added to the mixture at room temperature. The solutions were kept in a water bath at 35 °C, and hydrochloric acid (HCl) was added into the solution followed by addition of tetraethyl orthosilicate (TEOS). After that, the solutions were vigorously stirred for 24 h in a water bath at 35 °C. The precipitated products were filtered, dried, and washed with distilled water after further hydrothermal treatment at 100 °C for 24 h. Finally, products were dried at 80 °C for 12 h and calcined in air at 550 °C for 3 h.

2.2 Synthesis of mesoporous TMDCs

As shown in Fig. 1, mesoporous TMDCs of MoS_2, $MoSe_2$, WS_2 and WSe_2 with developed layered crystallinity were obtained *via* the nano-replication method with a melting-infiltration of chalcogen (S or Se) powders approach using bicontinuous cubic *Ia*3*d* structured KIT-6 silica as a hard-template. Phosphomolybdic acid hydrate ($H_3PMo_{12}O_{40} \cdot xH_2O$, Sigma-Aldrich, ACS reagent), phosphotungstic acid hydrate ($H_3PW_{12}O_{40} \cdot xH_2O$, Aldrich, reagent grade), sulphur (S, Sigma-Aldrich, purum p.a., ≥ 99.5%) and selenium (Se, Aldrich, ~100 mesh, 99.99% trace metal basis) were used as received without pre-treatment. For preparation of the mesoporous MoS_2 and $MoSe_2$, 0.85 g and 0.54 g of $H_3PMo_{12}O_{40} \cdot xH_2O$, respectively, were dissolved in 3.0 g of doubly distilled water solvent, and each solution was impregnated into the mesopore of 3.0 g of KIT-6 silica template by the incipient-wetness method. After evaporation of water solvent, 0.36 g of sulphur and 0.56 g of selenium powders were mixed with respective silica/precursor composites. The mixtures were kept at 160 or 240 °C for 12 hours in an autoclave for the melting infiltration of elemental sulphur or selenium within mesopores of the silica template containing transition metal precursors. Then, the composites were heated at 800 °C for 3 hours under an H_2 atmosphere for the crystallization of metal chalcogenides. The silica templates were almost perfectly etched by using 2 M NaOH aqueous solution. For the synthesis of the mesoporous WS_2 and WSe_2, 0.90 g and 0.65 g of $H_3PW_{12}O_{40} \cdot xH_2O$ were used with 0.23 g of sulphur and 0.42 g of selenium, respectively, as precursors, and other procedures were made in the same way as the synthesis of MoS_2 and $MoSe_2$.
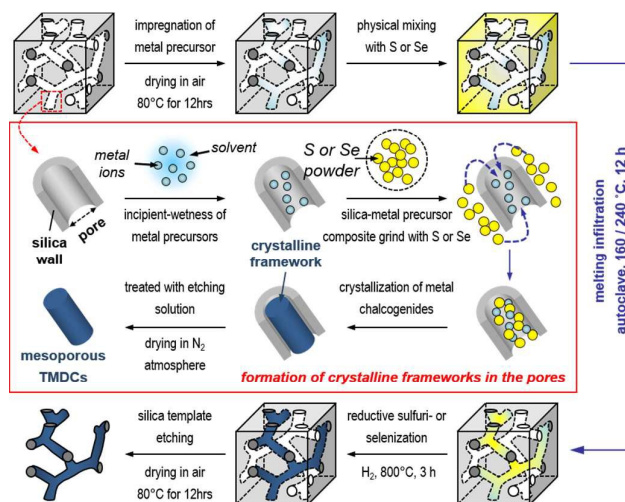
Fig. 1 A schematic illustration of melting-infiltration assisted nano-replication method for the synthesis of mesoporous TMDCs.

2.3 Characterization

Low-angle X-ray diffraction (XRD) patterns of the mesoporous silica KIT-6 were measured in transmittance mode using the Rigaku D/MAX-2500 equipped with Cu K_α radiation at an acceleration voltage of 40 kV and a current of 300 mA, and low- and wide-angle XRD patterns of the mesoporous TMDCs were obtained in reflection mode using a Rigaku Ultima IV equipped with Cu K_α at 40 kV and 30 mA. Raman spectrums were obtained by using WITEC α-300 Raman spectrometer with Ar ion laser of 532 nm at room temperature. N_2 adsorption-desorption isotherms were measured by the Micromeritics TriStar II series at liquid N_2 temperature. All of the samples were completely dried under vacuum at 100 °C for 24 h before taking measurements. The specific BET surface area was calculated from the adsorption branches in the range of p/p_0 = 0.05 – 0.20, and pore diameters were obtained using the BJH method. Scanning electron microscopy (SEM) images were taken using a JEOL JSM-7100F FE-SEM operating at an accelerating voltage of 15 kV. Transmission electron microscopy (TEM) images were obtained using a JEOL JEM 3010 at an acceleration voltage of 300 kV.

The electrochemical performances were characterized using a WBCS3000K8 battery test instrument (Won-A Tech powered by Zive Lab) at room temperature. The electrochemical lithium storage behaviours of the mesoporous TMDCs of ME_2 were observed using the half-cell test. In order to prepare the working electrode, active materials (mesoporous ME_2), conductive additives (Super P® carbon black, TimCal Graphite & Carbon) and binder (polyamide-imide polymers, PAI, Solvay, Torlon® 4000T) dissolved in N-methylpyrrolidone (NMP, 1-methyl-2-pyrrolidone, C_5H_9NO, Sigma-Aldrich, biotech. grade, ≥ 99.5%) at a typical weight ratio of 70 : 15 : 15 were casted on a copper (Cu) foil current collector. Afterwards, the electrodes were dried in a vacuum oven at 200 °C for 2 h, and CR2032 coin type cells were employed in the battery tests, with lithium foil serving as counter electrode and a porous Celgard 2400 polypropylene microporous membrane as separator. The electrolyte was 1.3 M $LiPF_6$ dissolved in ethyl carbonate (EC) and diethyl carbonate (DEC) mixture, in a volume ratio of 30:70.

3. Result and discussion

3.1 Characterization of mesoporous TMDCs

Mesoporous TMDCs ME_2 (M = Mo, W; E = S, Se) were obtained by the melting infiltration-assisted nano-replication route as depicted in Fig. 1. After loading metal precursors into the highly ordered mesoporous silica template (KIT-6, bicontinuous cubic $Ia3d$, see Fig. S1), elemental S and Se powders were impregnated through the melting infiltration method within mesopores. As shown in Fig. S2, diffraction peaks of crystalline sulphur powders completely disappear after the melting infiltration process, implying faithful dispersion of sulphur elements within mesopore of silica template.
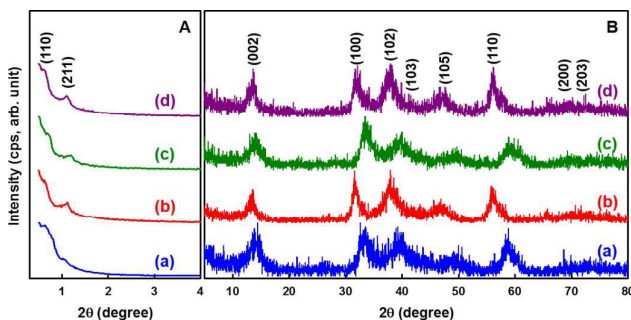
Fig. 2 (A) Low- and (B) wide-angle XRD patterns of the mesoporous (a) MoS_2, (b) $MoSe_2$, (c) WS_2, and (d) WSe_2.

Low-angle XRD patterns with two distinct peaks at around 0.65 ° and 1.10 °, which correspond to the (110) and (211) plane of the mesoporous TMDCs, are shown in Fig. 2A. The presence of the (110) diffraction peak presents mesostructural transformation from cubic $Ia3d$ of the KIT-6 silica template to tetragonal $I4_1/a$ or lower symmetry of the TMDC replica after the template removal process. Despite the use of the same KIT-6 silica as a hard-template, the peak positions of the mesoporous TMDCs are slightly different from each other, which may be due to the low ordering of the mesostructures of resulting materials.

The wide-angle XRD patterns of the mesoporous TMDCs in Fig. 2B show Bragg peaks corresponding to (002), (100), (102), (103), (105), (110), (200) and (203) reflection planes in the range of 10 – 80 °, which can be indexed to the hexagonal $P63/mmc$ 2H-syn structures as defined in JCPDS cards (PDF No. 87-2416 for MoS_2; 87-2419 for $MoSe_2$; 87-2417 for WS_2; and 87-2418 for WSe_2). Broad peaks in Fig. 2B may be attributed to the small grain sizes and nano-sized frameworks. The peak positions of the mesoporous TMDCs are almost identical, and could not be distinguished because of the equal ionic radii of Mo and W (115 pm) in hexagonal 2H-syn crystal phase. However, $MoS_2/MoSe_2$ and WS_2/WSe_2 are distinguishable in the XRD patterns, because the ionic radius of S (100 pm) in 2H-syn crystal structure differs from that of Se (115 pm). Note that impurity peaks could not be observed, suggesting that impregnated precursors were completely converted into the crystalline TMDC framework. The (002) peak positions of the mesoporous MoS_2 (14.01 °), $MoSe_2$ (13.55 °), WS_2 (14.19 °) and WSe_2 (13.70 °) were shifted to a lower angle region compared to the JCPDS values (PDF No. 87-2416 MoS_2 14.12 °; 87-2416 $MoSe_2$ 13.68 °; 87-2416 WS_2 14.32 °; and 87-2416 WSe_2 13.73 °), revealing a slight expansion in the interlayer distance of the (002) plane (MoS_2: mesoporous 0.632 nm, JCPDS 0.626 nm; $MoSe_2$: mesoporous 0.653 nm, JCPDS 0.647 nm; WS_2: mesoporous 0.624 nm, JCPDS 0.618 nm; WSe_2: mesoporous 0.646 nm, JCPDS 0.644 nm). The expanded interlayer distance of the mesoporous TMDCs could be attributed to the twisted or nano-sized crystal structure.[54] Raman spectroscopy studies also confirmed the 2H–syn layered crystal structure of mesoporous TMDCs with distinguishable peaks which corresponds

to 380 and 405 cm^{-1} for the E_{1g}^1 and A_{1g} of the MoS_2, 240 and 287 cm^{-1} for the A_{1g} and E_{1g}^1 of the $MoSe_2$, 347 and 417 cm^{-1} for the E_{1g}^1 and A_{1g} of the WS_2, and 249 cm^{-1} for the A_{1g} of the WSe_2.[60-64]
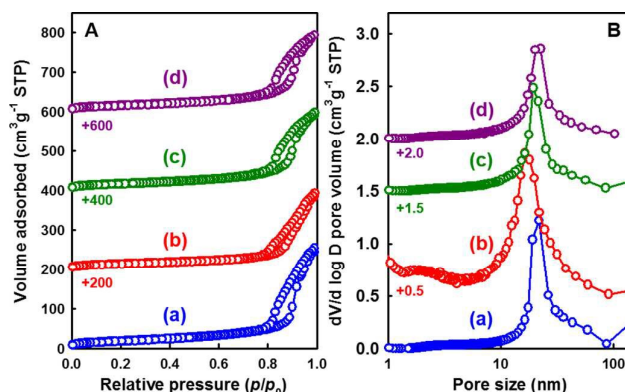
Fig. 3 N_2 adsorption-desorption isotherms (A), and the corresponding pore size distribution (B) of the mesoporous (a) MoS_2, (b) $MoSe_2$, (c) WS_2, and (d) WSe_2.

Table 1. Physical properties of the mesoporous TMDCs.

Material	S_{BET} (m^2/g)	V_{total} (cm^3/g)	D_p (nm)	d_{002} (Å) [a]	d_{002} (Å) [b]
(a) meso-MoS_2	87.3	0.25	21	6.32	6.26
(b) meso-$MoSe_2$	96.9	0.27	16	6.53	6.47
(c) meso-WS_2	97.4	0.23	19	6.24	6.18
(d) meso-WSe_2	105.0	0.21	22	6.46	6.44

[a] Calculated from the wide-angle XRD patterns in Fig. 2B. [b] Reference values given in the JCPDS cards.

The N_2 sorption isotherms of the mesoporous TMDCs in Fig. 3A show typical type IV isotherms with H1 hysteresis loop in the range of p/p_0 = 0.8 – 1.0, which are typical characteristics of mesoporous materials. The corresponding BJH pore size distribution curves calculated from the adsorption branches (Fig. 3B) show large pores of 16 – 22 nm. These large pore sizes of the mesoporous TMDCs support the phase transformation from cubic $Ia3d$ to tetragonal $I4_1/a$ or lower symmetry, which was expected from the low-angle XRD patterns (Fig. 2A). The mesoporous TMDCs also exhibit high specific BET surface areas and large total pore volumes as shown in Table 1.

As shown in the SEM images of Fig. 4A(a – d), the particle size of several micrometres and overall particle morphologies of mesoporous TMDCs are very similar to those of the KIT-6 silica template (see Fig. S1). The detailed porosities of the materials also can be confirmed by high resolution SEM (HR-SEM) studies as depicted in Fig. 4B(a – d). The structural ordering in several nano-meter scales of the mesoporous MoS_2 is presented in Fig. 4C(a). However, other materials exhibit disordered pore structures (Fig. 4C b – d). All of the mesoporous TMDCs display developed layered crystallinities as shown in Fig. 4D(a – d). The interlayer distances of the mesoporous MoS_2, $MoSe_2$, WS_2 and WSe_2 are 0.63 nm, 0.65 nm, 0.62 nm and 0.65 nm, respectively, which correspond to the interlayer distances between the E–M–E (E = S, Se; M = Mo, W) tri-layers of the hexagonal $P63/mmc$ 2H-syn crystal structure. These values are well matched with values from the wide-angle XRD patterns in Fig. 2B.

In order to compare electrochemical lithium storage behaviour of bulk and mesoporous TMDCs, bulk MoS_2 was purchased from Sigma-Aldrich. Fig. S5 shows that bulk MoS_2 also exhibits the

hexagonal *P*63/*mmc* crystal phase, particle size of several micrometres with 2-D sheet-like morphologies and a thickness of tens of nanometres from the SEM images in Fig. S5(c, d), and layered crystallinities (d_{002} = 0.63 nm) as shown in Fig. S5(f).
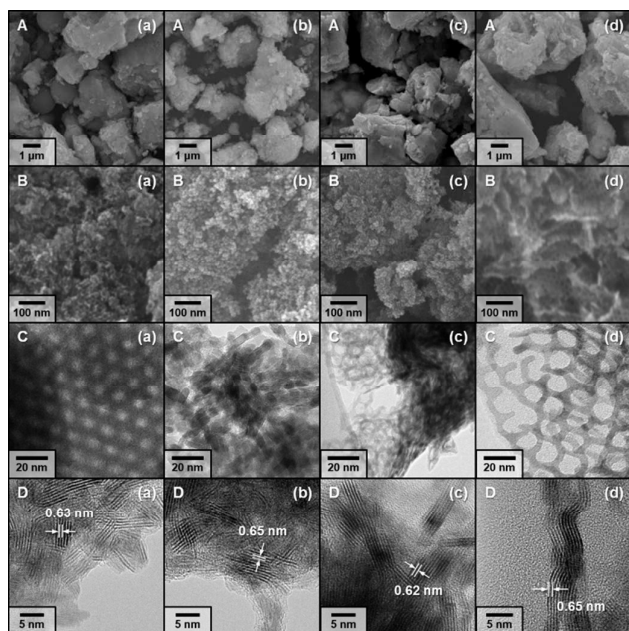
Fig. 4 (A) SEM, (B) HR-SEM, (C) TEM and (D) HR-TEM images of the mesoporous (a) MoS_2, (b) $MoSe_2$, (c) WS_2, and (d) WSe_2.

3.2 Electrochemical properties of the mesoporous TMDCs

The electrochemical properties of the electrode materials were studied using cyclic voltammetry (CV) and galvanostatic discharge–charge tests. Fig. 5(a) shows cyclic voltammogram of the mesoporous MoS_2 electrode at a scan rate of 0.05 mV·s^{-1} in the range of 0.01 – 3.00 V for the first five cycles. At the first cycle, two reduction peaks appeared at 1.05 and 0.25 V. The first reduction peak at 1.05 V could be assigned to lithium insertion into the interlayer of MoS_2, accompanied by phase transition from the 2*H* to 1*T* structure of Li_xMoS_2, *i.e.*, from trigonal prismatic to octahedral molybdenum coordination.[55, 65-67] The second reduction peak at 0.25 V could be ascribed to the reduction of Li_xMoS_2 to metallic Mo and Li_2S by conversion reaction. Two remarkable oxidation peaks appeared at 1.60 and 2.26 V, and the first oxidation peak may be related to partial oxidation of metallic Mo to MoS_2. However, the secondary oxidation peak at 2.26 V is not clearly defined yet. In the case of nano-structured MoS_2, the oxidation peak around this potential range is attributed to formation of MoS_2.[34, 66-68] In the cases of metal oxides and sulphides, electrochemical polarizations between the discharge–charge processes are typically *ca.* 1.0 and 0.6 V, respectively.[69, 70] Y.-S. Hu *et al.* suggested that the oxidation peak around 2.30 V is related to formation of sulphur rather than MoS_2, because if this oxidation peak represents the oxidation of Mo to MoS_2, polarization between the discharge and charge curves would be around 1.87 V, which is much higher than those commonly observed at transition metal oxides electrode.[55] At the second cycle, a new reduction peak appeared at 1.81 V and this peak shifted to 1.85 V for the 5th cycle, and this also supports the hypothesis that the oxidation peak at 2.26 V of the first cycle is related to the formation of sulphur.

The bulk MoS_2 electrode shows two reduction peaks at 0.85 V and 0.38 V for the first CV experiment as shown in Fig. 5(b). The first reduction peak corresponds to lithium intercalation and the second one is related to conversion of Li_xMoS_2 to Mo and Li_2S. However, in contrast to the mesoporous MoS_2, only one oxidation peak appeared at 2.31 V, which might be assigned to oxidation of Mo to MoS_2. From this cyclic voltammogram, one can reasonably expect that the oxidation of Mo and Li_2S to form MoS_2 simultaneously occurred in this one oxidation peak at 2.31 V. In the second cycle, a new reduction peak also appeared in the case of bulk MoS_2 at 1.88 V, and this peak shifted to 1.41 V in the 5th cycle. The reduction peak at 0.85 V observed in the first cycle was shifted to 1.10 V in the second cycle, which corresponds to lithium intercalation into the MoS_2 layer, and intensities gradually decrease with increases in cycle number.
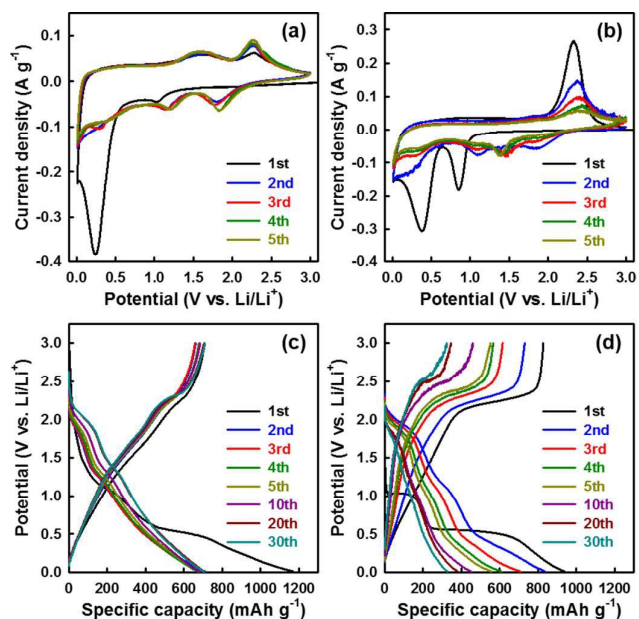
Fig. 5 (a, b) CV curves and (c, d) discharge-charge profiles of the (a, c) mesoporous MoS_2 and (b, d) bulk MoS_2.

Fig. 5(c) shows voltage profiles of the mesoporous MoS_2 electrode at a constant current rate of 0.1 C (1 C = 670 mAh·g^{-1} for MoS_2) in the range of 0.01 – 3.00 V. The first voltage plateau at 1.05 V might correspond to the reduction peak at 1.05 V of the cyclic voltammogram at the first cycle (Fig. 5(a)), and the capacity of this plateau is about 231.7 mAh·g^{-1} (1.38 mol of Li$^+$ uptake). The second plateau around 0.50 V might be associated with the second reduction peak observed at 0.25 V in the cyclic voltammogram, and the capacity at this plateau (0.5 - 0.43 V) is 735.7 mAh·g^{-1} corresponding to 4.4 mol of Li$^+$ uptake into the mesoporous MoS_2 electrode. The sloped region below 0.43 V has a capacity of 434.9 mAh·g^{-1}, which might be attributed to the formation of an SEI layer and/or lithium storage within the interfaces between two distinct phases of metallic Mo and Li_2S.[71] The voltage profile at the first cycle showed a reversible capacity of about 710 mAh·g^{-1} with an initial efficiency of 60.5 %, which is higher than the theoretical capacity of MoS_2 based on the conversion mechanism (670 mAh·g^{-1}). The low initial efficiency of the mesoporous MoS_2 electrode may be related to the formation of an SEI layer and/or the lithium storage reaction at the interface between Mo and Li_2S. Bulk MoS_2 showed a reversible capacity of about 828 mAh·g^{-1} with an initial efficiency of

88.4%, which is also higher than that of the meso-MoS$_2$. However, after the second discharge, no remarkable plateaus were observed and the reversible capacities dramatically decreased to 307.2 mAh·g^{-1} after 30 cycles.
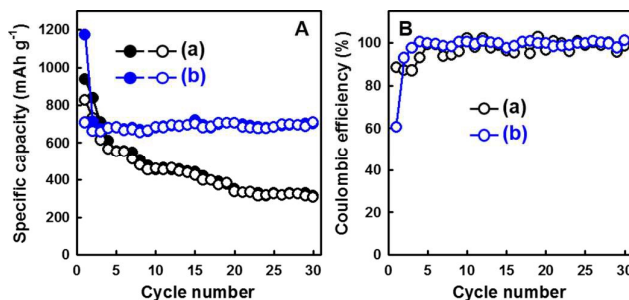
Fig. 6 (A) Cycling performance and (B) coulombic efficiency at 0.1 C of the (a) bulk MoS$_2$ and (b) mesoporous MoS$_2$.

Fig. 6A and 6B display cycling performance and coulombic efficiency of bulk and mesoporous MoS$_2$ electrodes. Bulk material exhibits unstable coulombic efficiencies during cycles, which are quite different from those of the mesoporous MoS$_2$ material. Compared to the bulk MoS$_2$, the present mesoporous MoS$_2$ electrode exhibits higher reversible specific capacity after the 30th cycle without capacity fading with almost constant coulombic efficiency of 99.3 % up to the 30th cycle. This improved electrochemical lithium storage performance of the meso-MoS$_2$ might be attributed to its unique mesostructure.

Fig. 7 shows the cyclic voltammogram and voltage profiles of the mesoporous MoSe$_2$, WS$_2$ and WSe$_2$ electrode during 30 cycles. The mesoporous MoSe$_2$ electrode shows similar cyclic voltammogram to that of MoS$_2$ (Fig. 7A). The first (0.69 V) and second (0.29 V) reduction peaks could be assigned to Li$^+$ insertion and the conversion reaction to form Mo and Li$_2$Se. Two representative oxidation peaks at 1.44 and 2.18 V could not be assigned exactly, but might be associated with the electrochemical oxidation of Mo to MoSe$_2$ and Li$_2$Se to Se, respectively. It should be noted that a new reduction peak appeared at 1.79 V (shifted to 1.88 V at the 5th cycle) at subsequent CV cycles, but was absent in the first cycle. This newly observed reduction peak might be coupled with the oxidation peak of 2.18 V (shifted to 2.21 V at 5th cycle) at the first cycle, which is related to the formation of Se rather than MoSe$_2$. These redox peaks in the cyclic voltammogram of mesoporous MoSe$_2$ are highly reversible in the following cycles.

Fig. 7(b) and 7(c) show the cyclic voltammogram of the mesoporous WS$_2$ and WSe$_2$ electrode, respectively, which are very similar to that of the mesoporous MoS$_2$ electrode. In the initial cycle of mesoporous WS$_2$, a reduction peak at 0.42 V is ascribed to the Li$^+$ intercalation, accompanied by the decomposition of the non-aqueous electrolyte.[56] At the first cycle, two remarkable oxidation peaks appeared at 1.72 and 2.35 V, which are associated with the oxidation of W to WS$_2$, and Li$_2$S to S, respectively. In the following cycles, new cathodic peaks could be also observed at 1.89 and 1.28 V, which shifted to lower potential compared to the first cycle. The intensities of the reduction peaks at 1.89 and 1.28 V slightly increase with cycling. The oxidation peak of 2.35 V would be related to the formation of S, likewise in case of mesoporous MoS$_2$. The cyclic voltammogram of mesoporous WSe$_2$ at the first cycle also shows two reduction peaks at 1.54 and 0.68 V, and two oxidation peaks at 1.08 and 2.12 V, respectively. The reduction peaks could be assigned to lithium insertion and conversion reaction containing

SEI layer formation, and oxidation peaks might be related to formation of WSe$_2$ and Se species. The cyclic voltammograms of mesoporous WS$_2$ and WSe$_2$ after the second cycle almost overlap, indicating excellent electrochemical reversibility of mesoporous electrodes.
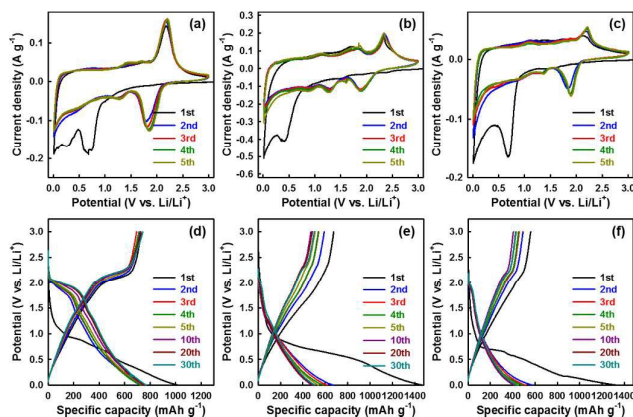
Fig. 7 (a, b, c) CV curves and (d, e, f) discharge-charge profiles of the mesoporous (a, d) MoSe$_2$, (b, e) WS$_2$, and (c, f) WSe$_2$.

Fig. 7(d) shows voltage profiles of the mesoporous MoSe$_2$ electrode at a constant current rate of 0.1 C (1 C = 422.3 mAh·g^{-1} for MoS$_2$) in the range of 0.01 – 3.00 V. The voltage profile at the first cycle showed a reversible capacity of about 728 mAh·g^{-1} with initial efficiency of 71.6 %, which is higher than the theoretical capacity of MoS$_2$ based on the conversion mechanism (422.3 mAh·g^{-1}). As mentioned earlier, the low initial efficiency of the mesoporous MoSe$_2$ electrode may also be attributed to electrochemical reaction at the low potential region.

Mesoporous WS$_2$ and WSe$_2$ electrodes show very similar voltage profiles to those of homologues containing Mo. As shown in Fig. 7(e) and 7(f), the reversible capacities of WS$_2$ and WSe$_2$ is 674.8 and 561.1 mAh·g^{-1}, respectively. These reversible capacities are much higher than the theoretical capacities of WS$_2$ and WSe$_2$ based on the conversion reaction mechanism (WS$_2$ 432.3; and WSe$_2$ 313.7 mAh·g^{-1}, based on conversion reaction). However, the initial coulombic efficiencies of W-containing mesoporous TMDCs are much lower than those of Mo-containing homologues (46.1 % for WS$_2$ and 42.4 % for WSe$_2$). These low coulombic efficiencies might be attributed to the initial sloped region at low potential range of the first discharge profiles shown in Fig. 5(c) and Fig. 7(d – f). In order to know precisely the main reason for the lower initial coulombic efficiency of W-containing mesoporous oxide materials, several spectroscopy studies are now underway.
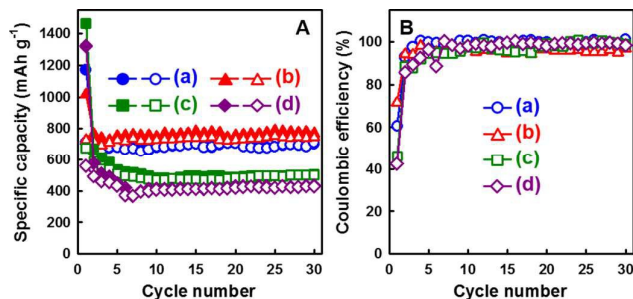
Fig. 8 (A) Cycling performance and (B) coulombic efficiency at 0.1 C of the mesoporous (a) MoS$_2$, (b) MoSe$_2$, (c) WS$_2$, and (d) WSe$_2$.

Fig. 8 shows cycling performance and coulombic efficiencies of mesoporous TMDC electrodes. As might be expected, mesoporous TMDC electrodes show highly stable capacity retention during 30 cycles. These excellent cycle performances originate from well-ordered mesoscale pores in the material, which act as a mechanical buffer to sustain the volume changes of the electrode material during cycling.
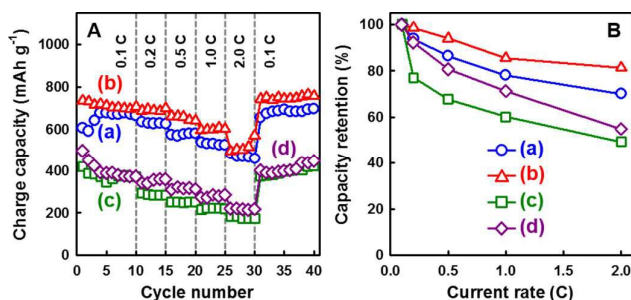
Fig. 9 (A) Rate capabilities and (B) capacity retention from 0.1 to 2 C of the mesoporous (a) MoS_2, (b) $MoSe_2$, (c) WS_2, and (d) WSe_2.

The rate capabilities of the mesoporous TMDCs electrodes from 0.1 to 2 C are given in Fig. 9. All mesoporous electrodes show very stable cycling performance at each applied current density, but the molybdenum-based electrodes exhibit much higher rate capability compared to tungsten-based electrodes in all regions. In particular, mesoporous $MoSe_2$ retained, even under a rate of 2 C, about 82% of the capacity at a 0.1 C rate. Excellent electrochemical performance including high capacities, highly stable cycle performances, and outstanding rate capabilities of the mesoporous TMDCs electrodes might be attributed to their high surface area, suitable pore sizes for diffusion of electrolyte, high activity, high electric and ionic conductivity, and short pathways for lithium insertion due to their nano-sized frameworks.

Conclusions

In conclusion, mesoporous transition metal dichalcogenide materials with good crystallinities were successfully obtained by the melting-infiltration assisted impregnation and nano-replication method. The mesoporous MoS_2, $MoSe_2$, WS_2 and WSe_2 electrodes achieved high reversible capacities and exhibited excellent high rate capabilities up to 2 C. High electrochemical performances of the present mesoporous electrodes may mainly come from high specific areas, large pore volumes, uniform pore sizes, and short pathways for lithium ion diffusion due to the nano-sized frameworks. These results imply that the mesoporous transition metal dichalcogenide materials could be promising for high power lithium ion batteries. We also expect that this simple synthesis strategy may be very useful for preparing mesoporous metal sulphides and selenides.

Acknowledgements

Notes and references

1. P. Poizot, S. Laruelle, S. Grugeon, L. Dupont and J. M. Tarascon, *Nature*, 2000, **407**, 496-499.
2. K. Zaghib, P. Charest, A. Guerfi, J. Shim, M. Perrier and K. Striebel, *Journal of Power Sources*, 2004, **134**, 124-129.
3. M. Armand and J. M. Tarascon, *Nature*, 2008, **451**, 652-657.
4. P. G. Bruce, B. Scrosati and J.-M. Tarascon, *Angewandte Chemie International Edition*, 2008, **47**, 2930-2946.
5. B. L. Ellis, K. T. Lee and L. F. Nazar, *Chemistry of Materials*, 2010, **22**, 691-714.
6. M. M. Thackeray, C. Wolverton and E. D. Isaacs, *Energy & Environmental Science*, 2012, **5**, 7854-7863.
7. S. Goriparti, E. Miele, F. De Angelis, E. Di Fabrizio, R. Proietti Zaccaria and C. Capiglia, *Journal of Power Sources*, 2014, **257**, 421-443.
8. H. Fujimoto, K. Tokumitsu, A. Mabuchi, N. Chinnasamy and T. Kasuh, *Journal of Power Sources*, 2010, **195**, 7452-7456.
9. J. Hou, Y. Shao, M. W. Ellis, R. B. Moore and B. Yi, *Physical Chemistry Chemical Physics*, 2011, **13**, 15384-15402.
10. J. Yang, X.-y. Zhou, J. Li, Y.-l. Zou and J.-j. Tang, *Materials Chemistry and Physics*, 2012, **135**, 445-450.
11. J. Yang, Y. Takeda, N. Imanishi, C. Capiglia, J. Y. Xie and O. Yamamoto, *Solid State Ionics*, 2002, **152–153**, 125-129.
12. C. K. Chan, X. F. Zhang and Y. Cui, *Nano Letters*, 2007, **8**, 307-309.
13. S. Boyanov, K. Annou, C. Villevieille, M. Pelosi, D. Zitoun and L. Monconduit, *Ionics*, 2008, **14**, 183-190.
14. C.-M. Park, J.-H. Kim, H. Kim and H.-J. Sohn, *Chemical Society Reviews*, 2010, **39**, 3115-3141.
15. L. Ji, Z. Lin, M. Alcoutlabi and X. Zhang, *Energy & Environmental Science*, 2011, **4**, 2682-2699.
16. T. Song, H. Cheng, H. Choi, J.-H. Lee, H. Han, D. H. Lee, D. S. Yoo, M.-S. Kwon, J.-M. Choi, S. G. Doo, H. Chang, J. Xiao, Y. Huang, W. I. Park, Y.-C. Chung, H. Kim, J. A. Rogers and U. Paik, *ACS Nano*, 2011, **6**, 303-309.
17. J. R. Szczech and S. Jin, *Energy & Environmental Science*, 2011, **4**, 56-72.
18. A. M. Chockla, K. C. Klavetter, C. B. Mullins and B. A. Korgel, *ACS Applied Materials & Interfaces*, 2012, **4**, 4658-4664.
19. M. Ge, J. Rong, X. Fang and C. Zhou, *Nano Letters*, 2012, **12**, 2318-2323.
20. J. Jiang, Y. Li, J. Liu, X. Huang, C. Yuan and X. W. Lou, *Advanced Materials*, 2012, **24**, 5166-5180.
21. C.-H. Lai, M.-Y. Lu and L.-J. Chen, *Journal of Materials Chemistry*, 2012, **22**, 19-30.
22. Z. Wang, L. Zhou and X. W. Lou, *Advanced Materials*, 2012, **24**, 1903-1911.
23. N. G. Rudawski, B. R. Yates, M. R. Holzworth, K. S. Jones, R. G. Elliman and A. A. Volinsky, *Journal of Power Sources*, 2013, **223**, 336-340.
24. K. Zhuo, M.-G. Jeong and C.-H. Chung, *Journal of Power Sources*, 2013, **244**, 601-605.
25. J. D. Benck, Z. Chen, L. Y. Kuritzky, A. J. Forman and T. F. Jaramillo, *ACS Catalysis*, 2012, **2**, 1916-1923.
26. S. Tongay, J. Zhou, C. Ataca, K. Lo, T. S. Matthews, J. Li, J. C. Grossman and J. Wu, *Nano Letters*, 2012, **12**, 5576-5580.

27. Q. H. Wang, K. Kalantar-Zadeh, A. Kis, J. N. Coleman and M. S. Strano, *Nature Nanotechnology*, 2012, **7**, 699-712.

28. C.-T. Li, C.-P. Lee, Y.-Y. Li, M.-H. Yeh and K.-C. Ho, *Journal of Materials Chemistry A*, 2013, **1**, 14888-14896.

29. C. Lin, X. Zhu, J. Feng, C. Wu, S. Hu, J. Peng, Y. Guo, L. Peng, J. Zhao, J. Huang, J. Yang and Y. Xie, *Journal of the American Chemical Society*, 2013, **135**, 5144-5151.

30. F. K. Perkins, A. L. Friedman, E. Cobas, P. M. Campbell, G. G. Jernigan and B. T. Jonker, *Nano Letters*, 2013, **13**, 668-673.

31. M. Sup Choi, G.-H. Lee, Y.-J. Yu, D.-Y. Lee, S. Hwan Lee, P. Kim, J. Hone and W. Jong Yoo, *Nat Commun*, 2013, **4**, 1624.

32. W. Wu, L. Wang, Y. Li, F. Zhang, L. Lin, S. Niu, D. Chenet, X. Zhang, Y. Hao, T. F. Heinz, J. Hone and Z. L. Wang, *Nature*, 2014, **514**, 470-474.

33. G. X. Wang, S. Bewlay, J. Yao, H. K. Liu and S. X. Dou *Electrochemical and Solid-State Letters*, 2004, **7**, A321-A323.

34. C. Feng, J. Ma, H. Li, R. Zeng, Z. Guo and H. Liu, *Materials Research Bulletin*, 2009, **44**, 1811-1815.

35. R. Bhandavat, L. David and G. Singh, *The Journal of Physical Chemistry Letters*, 2012, **3**, 1523-1530.

36. X. Fang, C. Hua, X. Guo, Y. Hu, Z. Wang, X. Gao, F. Wu, J. Wang and L. Chen, *Electrochimica Acta*, 2012, **81**, 155-160.

37. X. Fang, C. Hua, C. Wu, X. Wang, L. Shen, Q. Kong, J. Wang, Y. Hu, Z. Wang and L. Chen, *Chemistry – A European Journal*, 2013, **19**, 5694-5700.

38. Y. Liao, K.-S. Park, P. Singh, W. Li and J. B. Goodenough, *Journal of Power Sources*, 2014, **245**, 27-32.

39. T. Stephenson, Z. Li, B. Olsen and D. Mitlin, *Energy & Environmental Science*, 2014, **7**, 209-231.

40. H. Zhou, S. Zhu, M. Hibino, I. Honma and M. Ichihara, *Advanced Materials*, 2003, **15**, 2107-2111.

41. F. Jiao, K. M. Shaju and P. G. Bruce, *Angewandte Chemie International Edition*, 2005, **44**, 6550-6553.

42. J.-Y. Luo, J.-J. Zhang and Y.-Y. Xia, *Chemistry of Materials*, 2006, **18**, 5618-5623.

43. F. Jiao, J. Bao and P. G. Bruce, *Electrochemical and Solid-State Letters*, 2007, **10**, A264-A266.

44. F. Jiao and P. G. Bruce, *Advanced Materials*, 2007, **19**, 657-660.

45. K. M. Shaju, F. Jiao, A. Debart and P. G. Bruce, *Physical Chemistry Chemical Physics*, 2007, **9**, 1837-1842.

46. F. Jiao, J. Bao, A. H. Hill and P. G. Bruce, *Angewandte Chemie International Edition*, 2008, **47**, 9711-9716.

47. Y. Ren, A. R. Armstrong, F. Jiao and P. G. Bruce, *Journal of the American Chemical Society*, 2009, **132**, 996-1004.

48. Y. Shi, B. Guo, S. A. Corr, Q. Shi, Y.-S. Hu, K. R. Heier, L. Chen, R. Seshadri and G. D. Stucky, *Nano Letters*, 2009, **9**, 4215-4220.

49. J. K. Shon, H. Kim, S. S. Kong, S. H. Hwang, T. H. Han, J. M. Kim, C. Pak, S. Doo and H. Chang, *Journal of Materials Chemistry*, 2009, **19**, 6727-6732.

50. W. Yue, C. Randorn, P. S. Attidekou, Z. Su, J. T. S. Irvine and W. Zhou, *Advanced Functional Materials*, 2009, **19**, 2826-2833.

51. W. Yue, X. Xu, J. T. S. Irvine, P. S. Attidekou, C. Liu, H. He, D. Zhao and W. Zhou, *Chemistry of Materials*, 2009, **21**, 2540-2546.

52. Y. Ren, L. J. Hardwick and P. G. Bruce, *Angewandte Chemie International Edition*, 2010, **49**, 2570-2574.

53. D. Saikia, T.-H. Wang, C.-J. Chou, J. Fang, L.-D. Tsai and H.-M. Kao, *RSC Advances*, 2015, **5**, 42922-42930.

54. Y. Shi, Y. Wan, R. Liu, B. Tu and D. Zhao, *Journal of the American Chemical Society*, 2007, **129**, 9522-9531.

55. X. Fang, X. Yu, S. Liao, Y. Shi, Y.-S. Hu, Z. Wang, G. D. Stucky and L. Chen, *Microporous and Mesoporous Materials*, 2012, **151**, 418-423.

56. H. Liu, D. Su, G. Wang and S. Z. Qiao, *Journal of Materials Chemistry*, 2012, **22**, 17437-17440.

57. H. Liu, D. Su, R. Zhou, B. Sun, G. Wang and S. Z. Qiao, *Advanced Energy Materials*, 2012, **2**, 970-975.

58. Y. Shi, C. Hua, B. Li, X. Fang, C. Yao, Y. Zhang, Y.-S. Hu, Z. Wang, L. Chen, D. Zhao and G. D. Stucky, *Advanced Functional Materials*, 2013, **23**, 1832-1838.

59. F. Chen, J. Wang, B. Li, C. Yao, H. Bao and Y. Shi, *Materials Letters*, 2014, **136**, 191-194.

60. J. Kibsgaard, Z. Chen, B. N. Reinecke and T. F. Jaramillo, *Nature Materials*, 2012, **11**, 963-969.

61. P. Tonndorf, R. Schmidt, P. Böttger, X. Zhang, J. Börner, A. Liebig, M. Albrecht, C. Kloc, O. Gordan, D. R. T. Zahn, S. Michaelis de Vasconcellos and R. Bratschitsch, *Opt. Express*, 2013, **21**, 4908-4916.

62. W. Zhao, Z. Ghorannevis, K. K. Amara, J. R. Pang, M. Toh, X. Zhang, C. Kloc, P. H. Tan and G. Eda, *Nanoscale*, 2013, **5**, 9677-9683.

63. M. Shanmugam, R. Jacobs-Gedrim, E. S. Song and B. Yu, *Nanoscale*, 2014, **6**, 12682-12689.

64. S.-Y. Chen, C. Zheng, M. S. Fuhrer and J. Yan, *Nano Letters*, 2015, **15**, 2526-2532.

65. E. Benavente, M. A. Santa Ana, F. Mendizábal and G. González, *Coordination Chemistry Reviews*, 2002, **224**, 87-109.

66. Q. Wang and J. Li, *The Journal of Physical Chemistry C*, 2007, **111**, 1675-1682.

67. G. Du, Z. Guo, S. Wang, R. Zeng, Z. Chen and H. Liu, *Chemical Communications*, 2010, **46**, 1106-1108.

68. J. Xiao, D. Choi, L. Cosimbescu, P. Koech, J. Liu and J. P. Lemmon, *Chemistry of Materials*, 2010, **22**, 4522-4524.

69. A. Débart, L. Dupont, R. Patrice and J. M. Tarascon, *Solid State Sciences*, 2006, **8**, 640-651.

70. B. Zhang, X. Qin, G. R. Li and X. P. Gao, *Energy & Environmental Science*, 2010, **3**, 1531-1537.

71. J. Jamnik and J. Maier, *Physical Chemistry Chemical Physics*, 2003, **5**, 5215-5220.

RSC Advances Accepted Manuscript

Graphical Abstract

Mesoporous transition metal dichalcogenides with 2D layered crystallinity, synthesized through a melting-infiltration assisted nano-replication, exhibit excellent electrochemical performances for lithium-storage.